Chapter 2

Real-Time Software-Defined Adaptive MIMO Visible Light Communications

Peng Deng

Additional information is available at the end of the chapter

http://dx.doi.org/10.5772/intechopen.68919

Abstract

Visible light communications (VLC) based on light-emitting diodes (LEDs) merges lighting and data communications in applications of Internet-of-Things and 5G networks. However, phosphor-based white LED has a limited linear dynamic range and limited modulation bandwidth. In practical indoor mobile communications, complex channel conditions change dynamically in real-time, and line of sight (LOS) links may be blocked by obstructions. We propose a real-time software-defined adaptive multi-input multi-output (MIMO) VLC system, that both modulation formats (QPSK,16-QAM,64-QAM, 256QAM) and MIMO reconfigurations (Spatial Diversity and Spatial Multiplexing) are dynamically adapted to the changing channel conditions, for enhancing both link reliability and spectral efficiency. Real-time and software defined digital signal processing (DSP) are implemented by Field Programmable Gate Array (FPGA) based Universal Software Radio Peripheral (USRP) devices. We theoretically analysed and experimentally evaluated nonlinear electrical-optical properties and modulation characteristics of white LEDs. We demonstrated a real-time Single-Carrier 256-Quadrature Amplitude Modulation (QAM) 2×2 MIMO VLC, achieving 1.81% averaged error vector magnitude (EVM), 2×10^{-5} bit error rate (BER) after 2 m indoor transmission. As an obstacle moved across LOS links, real-time software-defined adaptive MIMO VLC system enhanced average error-free spectral efficiency of 12 b/s/Hz. This will provide high throughputs for robust links in mobile shadowing environments.

Keywords: visible light communications, light-emitting diodes, multi-input multi-output, spatial multiplexing, spatial diversity, link adaptation, software-defined, channel capacity, nonlinear modulation, equalization, constellation optimization, synchronization

1. Introduction

The world growth in wireless mobile data traffic has led to the development of new technologies for high capacity and energy-efficient wireless communication systems. This fact results in an increasing throughput requirement from the next generation mobile communication networks (5G), which are expected to address several critical challenges, such as broadband capacity, spectral efficiency, power efficiency, quality of services, and mobility coverage. Visible light communication (VLC) system has been accepted as part of the 802.15.7 task group and proposed as a supplement technology in 5G networks standards. VLC based on light-emitting diodes (LEDs) merge lighting and data communications in applications due to their energy efficiency, spectral efficiency, security, and reliability [1]. The white light LEDs have advantages of long lifetime, energy-efficient, and environmental friendliness. VLC using lighting LEDs could provide many advantages, such as no electromagnetic interference (EMI), integration with indoor lighting, available worldwide, and unlicensed bandwidth [2]. The VLC application shown in **Figure 1** is relevant to aerospace, automotive, healthcare industries, 5G networks, wireless personal area networks (WPANs), Internet-of-Things, and ad-hoc networks, as it focuses on the development of radio frequency (RF)-interference-free high-bandwidth communication networks using white light LEDs.

The commercial white light LED utilized for general lighting is mostly based on a blue LED chip covered by a phosphor layer rather than red-green-red (RGB) LEDs, as phosphor white LEDs have much lower complexity and cost. However, phosphor-LEDs have limited modulation bandwidth due to the phosphorescent components. Several modulation bandwidth extension technologies have been investigated, such as optical blue filtering, analogue equalizer, and digital equalization [3]. However, optical filtering of blue light causes large optical intensity loss and decreases visible light transmission range.

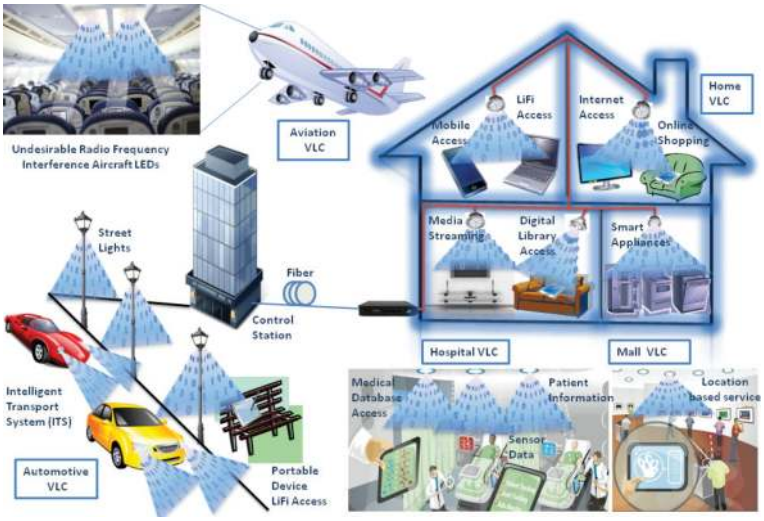

Figure 1. Visible light communication applications.

The capacity of the VLC system under the limited bandwidth can be enhanced by using high spectrally efficient modulation formats, such as orthogonal frequency-division multiplexing (OFDM) [4], Nyquist single-carrier modulation, and carrier-less amplitude and phase (CAP) modulation [5]. Using bit- and power-loading techniques, OFDM can maximize the transmission capacity under the constraint bit error rate (BER). However, high peak-to-average-power ratio (PAPR) of OFDM signal is the crucial challenge for the limited linear dynamic range of white LEDs and nonlinear modulation characteristics in the VLC system [6, 7]. Implementation of real-time CAP systems requires relatively high speed and high-resolution analog to digital converter (ADC), which suffers from high sampling jitter sensitivity. Quadrature amplitude modulation (QAM) architectures have tolerances to nonlinear distortions and sampling jitter. Despite the complexity of adding analog multipliers, QAM systems reduce the sampling rate and resolution requirements of A/Ds for real-time applications.

Moreover, LED-based VLC naturally constitutes a multi-input multi-output (MIMO) system, as large numbers of lighting lamps made up of multiple LEDs are provided by indoor illumination systems [8]. MIMO transmission techniques can be classified by spatial diversity, spatial multiplexing, and spatial modulation. Note that 4×9 spatial multiplex MIMO VLC using 16-QAM OFDM is demonstrated at 250 Mb/s per channel over 1 m range [9]. And 4×4 spatial multiplex MIMO VLC using OOK modulation achieved a data rate of 50 Mb/s over 2 m [10]. Also, 2×2 MIMO VLC using 4-QAM Nyquist single-carrier with frequency domain equalization is demonstrated at 500 Mb/s in 40-cm transmission distance [11]. A wide filed-of-view receiver using fisheye lens is proposed in the spatial-diversity MIMO VLC system [12, 13].

However, most MIMO VLC systems currently manifest the fixed MIMO technology, static channel condition estimation, and offline signal processing. In fact, complex channel conditions are expected to be changed dramatically, and spectral efficiency must be optimized adaptively in practical indoor wireless mobile communications [14, 15]. For example, the MIMO VLC system using fixed spatial multiplexing will suffer link interruption, once any sub-channel condition becomes degraded [16, 17]. Real-time data processing on field programmable gate arrays (FPGAs) based software-defined device can build a fully real-time reconfigurable and an adaptive optical wireless system by upgrading the software [18, 19]. The network architecture should also be designed to support the adaptive MIMO schemes with distributed smart antenna systems [20, 21]. Thus, a real-time adaptive MIMO optical wireless system is necessary to deal with the dynamic complex channel conditions and enhance the robust mobility and link reliability in future wireless mobile networks.

In this chapter, we propose an adaptive MIMO VLC solution that both modulation schemas and MIMO schemas are dynamically adapted to the changing channel conditions for enhancing error performance and spectral efficiency. We experimentally demonstrate a real-time software-defined single-carrier M-QAM MIMO VLC system by using link adaptation of spatial multiplexing and spatial diversity. The VLC transceivers use independent phosphor-white LEDs and PIN photodetectors without blue filtering. We theoretically analyze and experimentally evaluate nonlinear electrical-optical properties and nonlinear modulation characteristics of white LEDs in the VLC system. LED nonlinear modulation characteristics reveal that the optimized LED drive current that corresponds to minimum BER increases with an increase in data rate. We explore FPGA-based universal software radio peripheral devices for real-time

digital signal processing. Software-defined implantation of MIMO VLC can enable an adaptive and reconfigurable communication system without hardware changes. We measured the error vector magnitude (EVM), bit error rate (BER), and spectral efficiency performance for single-carried M-QAM MIMO VLC using spatial diversity and spatial multiplexing. Results show that spatial diversity MIMO VLC improves error performance at the cost of spectral efficiency that spatial multiplexing should enhance. With an obstacle moving across line-of-sight (LOS) links, the average error-free spectral efficiency of adaptive 2 × 2 MIMO VLC achieved 12 b/s/Hz over 2 m indoor dynamic transmission after an obstruction. Real-time software-defined adaptive MIMO VLC will enhance spectral efficiency and link reliability in a mobile environment with shadowing.

2. Nonlinear modulation characteristics of white LED in VLC system

Nonlinear modulation characteristics and limited linear dynamic range of white LEDs are dependent on drive currents, which determine VLC system performance. The static nonlinear LED transfer functions for voltage or optical power to current conversion [22] take into account just clipping effects or continuous-gradient nonlinearity [6]. Moreover, the approximating polynomial model of LED nonlinearity is only valid for small modulation frequencies [6]. Thus, we theoretically analyze a complete nonlinear modulation model based on rate equation [7] and experimentally evaluate the effect of LED drive current on nonlinear modulation characteristics of VLC system [23].

2.1. Nonlinear electrical-optical characteristics of white LED

LEDs are nonlinear devices such as the series resistance and capacitance depend strongly on the bias current. A nonlinear resistor represents the *I-V* characteristic of the LED by the Shockley equation [24]. $i_d = I_0\left[\exp\left(qv_d/nkT\right) - 1\right]$, where k is the Boltzmann's constant, q is the electron charge, T is the junction temperature, n is the diode ideality factor, and v_d is the junction voltage. The factor n is approximately 2 for an InGaN LED. I_0 is the reverse saturation current [24].

However, the LED nonlinear *I-V* characteristic needs to be modified in order to take into account parasitic resistances. A series resistance can be caused by excessive contact resistance or by the resistance of the neutral regions [24]. The equivalent circuit for the transient behavior of LED is shown in **Figure 2**. Considering the nonlinear series resistances R_s and parallel resistance R_p of LED, the *I-V* characteristic of a forward-biased p-n junction diode ($v_d = v\text{-}IR_s$, $v_d \gg (kT/q)$ is given by $I - (v - IR_s)/R_p = I_0 \exp\left[q(v - IR_s)/(nkT)\right]$. For devices with a high parallel resistance ($Rp \to \infty$), the diode *I-V* characteristic can be written as

$$I = I_0 \exp\left[e(v - IR_s)/(nkT)\right] \tag{1}$$

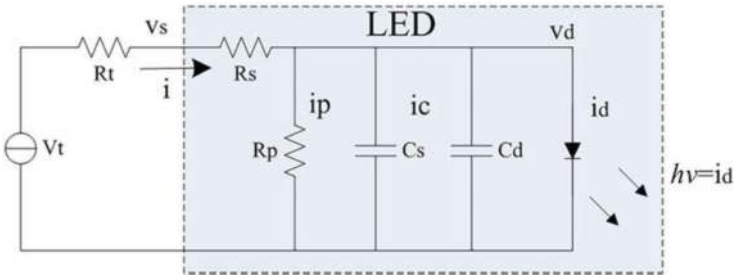

Figure 2. The equivalent circuit for the transient behavior of LED.

For $Rp \rightarrow \infty$ and $Rs \rightarrow 0$, this equation reduces to the Shockley equation.

We measured electrical-optical properties of LED chips. **Figure 3(a)** shows experimental and theoretical relationship between drive current I against forward voltage v for a single LED. The measured LED bias current I against the junction voltage v_d characteristic well matches the theoretical nonlinear I-v_d model. **Figure 3(b)** shows relationship between optical power and forward voltage for a single LED. LED optical power get cut off below the threshold of 10 mA @ 2.7 V, increased within a linear dynamic range of 600 mV around bias point of 450 mA @ 3.3 V, finally saturated and decreased beyond 1100 mA @ 3.7 V. This is because nonlinear thermal effects appear to reduce the internal quantum efficiency and electrical to optical conversion efficiency. Thus, the LED drive current and linear dynamical range should be optimally designed to avoid nonlinear distortions in output optical power and degradations in VLC performance [7].

Figure 4 shows LED bias current and output optical power against forward voltage for two parallel-connected and series-connected LED chips. It can be seen that the nonlinear region of parallel-connected LED chips fluctuates dramatically above 3000 mA @ 3.5 V due to the larger forward current thermal effect, whereas the linear modulation dynamic range of the series-connected LED chips increases to 1200 mV around the optimal DC-bias point 370 mA @ 6.4V due to the improved impedance. Thus, series-connected LED chips can enhance the linear dynamic range.

We evaluated VLC transceiver system response at the frequency of 10 MHz along the distance of 1 m. Using the same transmitter signal amplitude of 100 mV, we measured the receive signal amplitude for different LED DC-bias power levels. **Figure 5** shows the effect of LED forward voltage and current on the AC signal system response for two and three series-connected LED chips. It is shown that the received signal and system response fluctuate to decline gradually with the increase of LED DC-bias current and voltage, because high DC power will lead to a nonlinear thermal effect that saturated output optical power and degraded AC signal amplitude. As compared, a larger number of series-connected LED chips can mitigate the nonlinear fluctuation of system response.

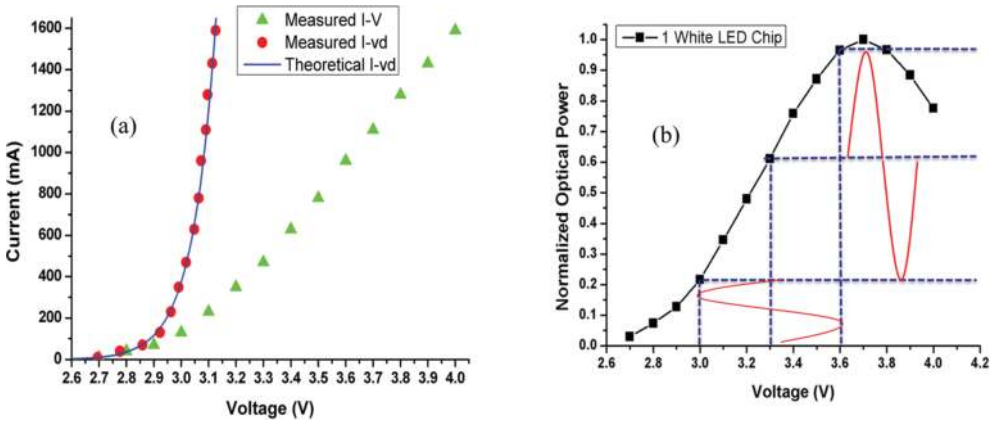

Figure 3. Electrical to optical properties of white LED. (a) DC-bias current against forward voltage and (b) normalized optical power against forward voltage for single LED.

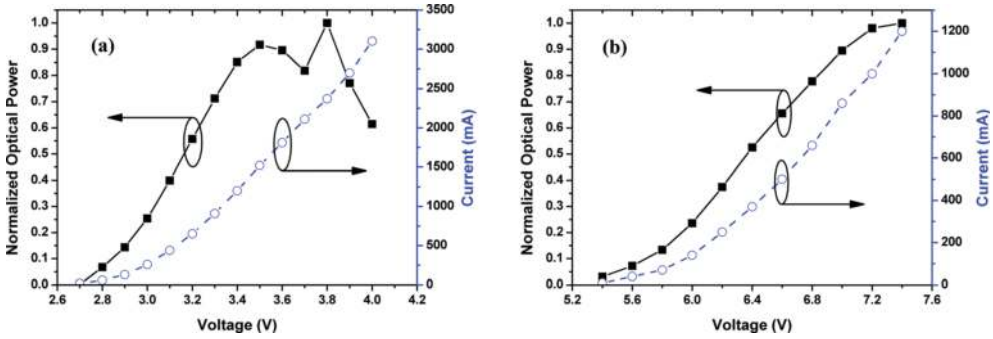

Figure 4. DC-bias current and normalized optical power against forward voltage for (a) two parallel connected LEDs and (b) two series-connected LEDs.

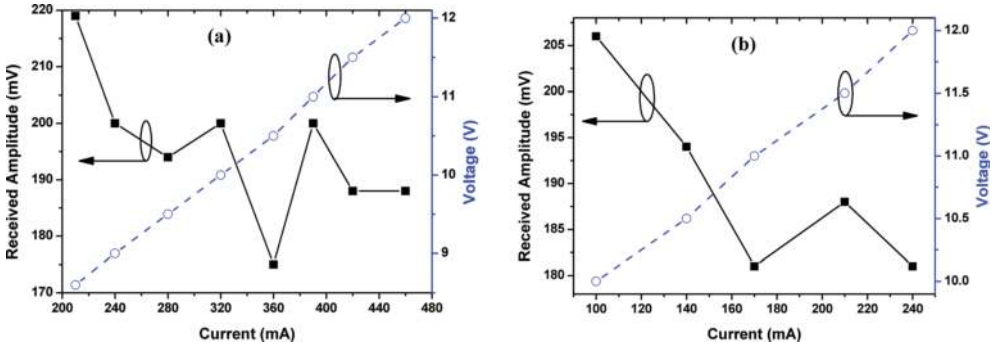

Figure 5. DC-bias current and voltage effect on VLC system response for (a) two series-connected LED chips and (b) three series-connected LED chips. Transmitter signal amplitude is 100 mV.

2.2. Nonlinear modulation bandwidth of white LED

2.2.1. LED modulation bandwidth due to carrier lifetime

The differential carrier lifetimes in InGaN-based LEDs can be described by the simple ABC model. This rate equation model considers that the current through the device is made up of three contributions: a nonradiative current I_A due to Shockley-Read-Hall (SRH) recombination at defect sites, a current I_B due to radiative recombination of electrons and holes, and an Auger current I_C due to cubic nonradiative recombination [25]. The total current is thus

$$I = I_A + I_B + I_C = qsd(\mathrm{AN} + \mathrm{BN}^2 + \mathrm{CN}^3) \tag{2}$$

where I is the operation current, q is the elementary charge, s and d are the device area and total thickness of the quantum wells (QWs), N is the carrier density, A, B, and C are the coefficients of Shockley-Read-Hall (SRH), radiative recombination and Auger nonradiative recombination.

Under small-signal modulation conditions, the luminescence decay is mono-exponential with the differential time constant [26]. The differential lifetime is then given by the derivative of the recombination rate with respect to carrier density $1/\tau_s = A + \mathrm{BN} + \mathrm{CN}^2$. In the case that linear and quadratic terms dominate the recombination rate, the simplified expression between carrier lifetime and bias current can be derived by $1/\tau_s^2 = A^2 + 4BI/qV$. Thus, the LED electrical-optical 3-dB bandwidth [23] related to the differential lifetime can be obtained

$$f_s = \frac{1}{2\pi\tau_s} = \frac{1}{2\pi}\sqrt{A^2 + \frac{4B}{qV}I} \tag{3}$$

2.2.2. LED modulation bandwidth due to space-charge capacitance

The common feature of LED is that the large junction over the entire wafer presents a space-charge capacitance of the junction in parallel with the diffusion capacitance of carrier lifetime. **Figure 2** shows the equivalent circuit for the transient behavior of LED. In addition to the diffusion capacitance C_d of carrier lifetime, there is the space-charge capacitance Cs of the depletion layer. The space-charge capacitance [27] is given by $C_s = C_0/\left(1 - v_d/\phi\right)^m$, where $C_0 = sc_0$, c_0 is the zero-bias capacitance per unit area, $\varnothing$ is the barrier voltage, and the exponent m is 1/2. The LED resistance R_s in the equivalent circuit accounts for the series resistance of the bulk material and the contact resistances. Thus, the time constant due to the space-charge capacitance [23] is given by $\tau_c = C_sR_s = R_sC_0/\left(1 - v_d/\phi\right)^m$. The electrical-optical 3-dB bandwidth related to space-charge capacitance can be obtained

$$f_c = \frac{1}{2\pi\tau_c} = \frac{\left(1 - v_d/\phi\right)^m}{2\pi R_sC_0} \tag{4}$$

2.2.3. Nonlinear modulation bandwidth of white LED

Considering the nonlinear electrical-optical characteristics of LED, substituting Eq. (1) into Eq. (4), the total LED rise time due to carrier spontaneous lifetime and space-charge capacitance [23] can be defined by

$$\tau_{\mathrm{LED}}(I) = \tau_s + \tau_c = \frac{1}{\sqrt{A^2 + 4BI/qV}} + \frac{R_s C_0}{\sqrt{1 - \ln(I/I_0)nkT/q\phi}} \tag{5}$$

The total equivalent electrical-optical 3-dB bandwidth due to the differential lifetime and space-charge capacitance can be expressed by the LED bias current

$$f_{\mathrm{LED}}(I) = \frac{1}{2\pi(\tau_s + \tau_c)} = \frac{1}{2\pi} \frac{\sqrt{(A^2 + 4BI/qV)[1 - \ln(I/I_0)nkT/q\phi]}}{\sqrt{1 - \ln(I/I_0)nkT/q\phi} + R_s C_0 \sqrt{A^2 + 4BI/qV}} \tag{6}$$

We measured the optical spectrum of different phosphor white LED chips (Osram Ostar) as shown in **Figure 6**. It can be seen that a commercial warm white LED (CWLED) contains only 10% blue component of the overall emitted power, while the emitted ultra-white LED light (UWLED) consists of 41% blue component and less slow yellow component from the phosphor. As the modulation bandwidth of blue light is higher than that of yellow component, the ultra-white LED (UWLED) can be used to improve the modulation bandwidth efficiency [7].

The effect of LED DC-bias current on electrical-optical-electrical (EOE) channel frequency response of the VLC transceiver is shown in **Figure 7**. The magnitude of the channel frequency response is measured by a network analyzer. It can be seen that the magnitude of frequency response reduced when bias current is less than 100 mA due to clipping of the lower peaks at the turn on point. For small frequency signals less than 10 MHz, VLC system frequency response

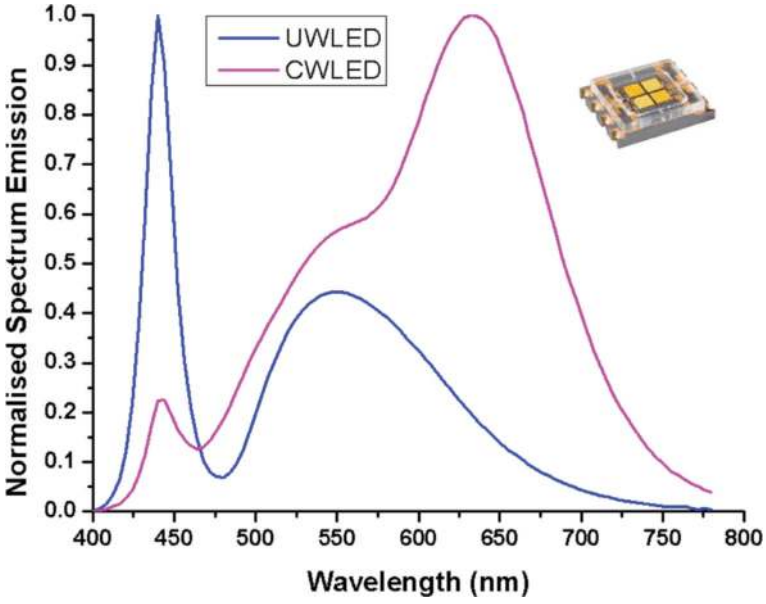

Figure 6. The measured optical spectrum of different white LED chips, inset: Osram white LED.

magnitudes reduce as LED bias currents increase, due to nonlinear intensity saturation at large currents. However, for high frequency signals in **Figure 7(b)**, the system response improves with the increasing DC bias current due to higher optical power detected at the receiver [7].

The comparison of experimental and theoretical relationship between 3-dB bandwidth of the VLC system and LED bias current is shown in **Figure 8**. It is found that the 3-dB bandwidth of the VLC system increases with LED bias current, because the bandwidth due to carrier lifetime *fs* in Eq. (3) increases significantly with carrier density and driving current. Furthermore, the LED bandwidth saturates and approaches to 7 MHz when DC bias current is larger than 250 mA, because the bandwidth due to space-charge capacitance f_c in Eq. (4) reduces apparently with bias current. It is shown that results of experimental measurement of LED bias current-related equivalent bandwidth well match the theoretical results in Eq. (6). Since the receiver itself has a relatively large bandwidth (photodetector 150 MHz, amplifier 1 GHz), the system bandwidth (7 MHz) is limited by the LED module.

As the blue filtering introduces high optical power attenuation, we extend LED modulation bandwidth without blue filtering. The magnitude of the channel frequency response was measured by a network analyzer. A first-order equalizer that consists of a capacitor in parallel with a resistor ($R = 1$ kΩ, $C = 30$ pF) is developed to enhance the system bandwidth. **Figure 9** presents the frequency response of the equalizer and the corresponding equalized VLC transceiver system. It can be seen that the optimized analogue equalizer can extend the bandwidth of the VLC transceiver from 7 to 40 MHz.

2.3. Nonlinear modulation effects of white LED on VLC performance

Figure 10 presents a diagram of experimental measurement setup for the VLC system. The analogue transmitter front-end superimposed the amplified output signal onto LED bias current using a bias-tee. The phosphorescent white LED (Osram OSTAR) with four chips provided 520-lm luminous flux with a 120° opening angle at 700 mA current. An aspheric lens collimated LED light propagation along line-of-sight paths. A high-speed PIN photodetector captured LED light by an aspheric convex lens. A low noise transimpedance amplifier (TIA)

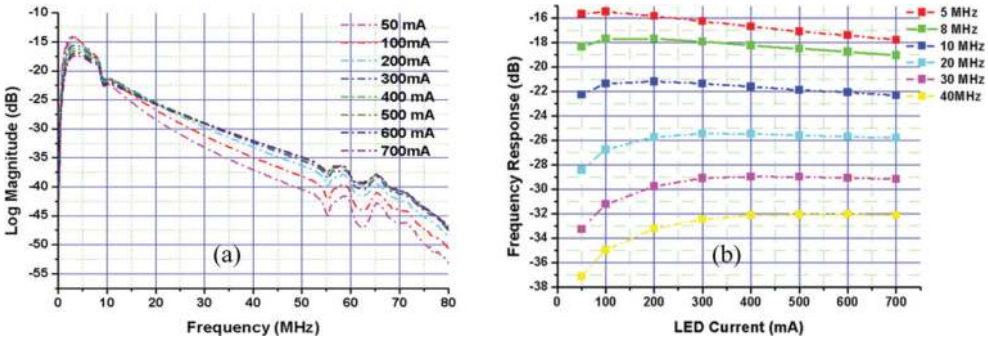

Figure 7. (a) The measured EOE channel frequency response of VLC transceiver for different LED DC bias currents and (b) frequency response versus LED DC bias current for different frequency.

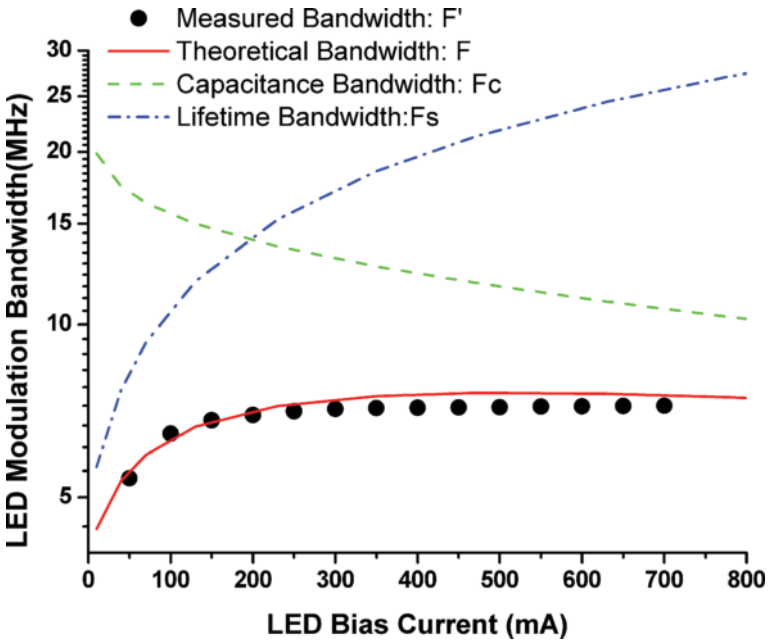

Figure 8. Relationship between 3-dB bandwidth and average LED current.

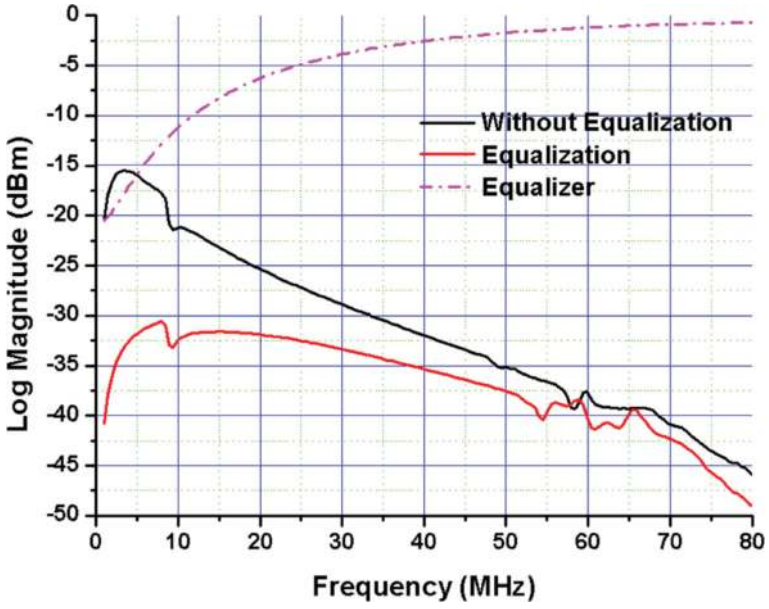

Figure 9. Electrical-optical-electrical system frequency response of VLC transceiver without equalization, VLC transceiver with equalization and the analogue equalizer.

amplified the photocurrent signal, which bandwidth was extended by a first-order analogue postequalizer [16]. The received electrical signal was amplified and then connected to a digital oscilloscope (HP 4396B) and a bit error rate tester (BERT).

A pseudorandom binary sequence (PRBS)-10 OOK-NRZ data stream with a peak-to-peak voltage swing of 2.5 V is used to modulate a single LED light. **Figure 11** shows the relationship between the measured bit-error-rate (BER) performance and the date rate of the equalized VLC system for different DC bias currents. It can be seen that the maximum date rate at DC bias current of 510 mA can achieve 60 Mbps for a BER threshold of 10^{-3}. In contrast, BER performance degraded obviously for both a low DC bias current of 200 mA and a high DC bias current of 680 mA.

The effect of LED DC bias current on VLC BER performance for different data rates is illustrated in **Figure 12**. For a BER threshold of 10^{-3}, the maximum date rate of 60 Mbps can be achieved at 510 mA bias current. The smaller bias currents less than 100 mA increased the BER at low data rates (20 and 32 Mbps). The DC bias current that corresponds to minimal BER value is used to identify the optimum bias point, where the LED is operating in a linear region with less probability of clipping the signal peaks. The high BER observed at the large bias current more than 200 mA is mainly due to the nonlinear thermal effect and the clipping of the upper peak at the maximum output optical power [7]. For high data rates (40 and 60 Mbps), BER decreases to the minimum value with an increase in LED bias current. This is because relatively high levels of optical power are required to overcome the received signal-to-noise penalty at a high data rate. Therefore, the optimized DC-bias current of an LED driver that corresponds to minimum BER increases gradually with an increase in the data rate. The modulation bandwidth can be enhanced by reducing parasitic resistances and capacitances of LED, or carrier sweep-out of the active region. This can help in controlling the dimmable illumination brightness of white LEDs to match the modulation speed and improve system performance.

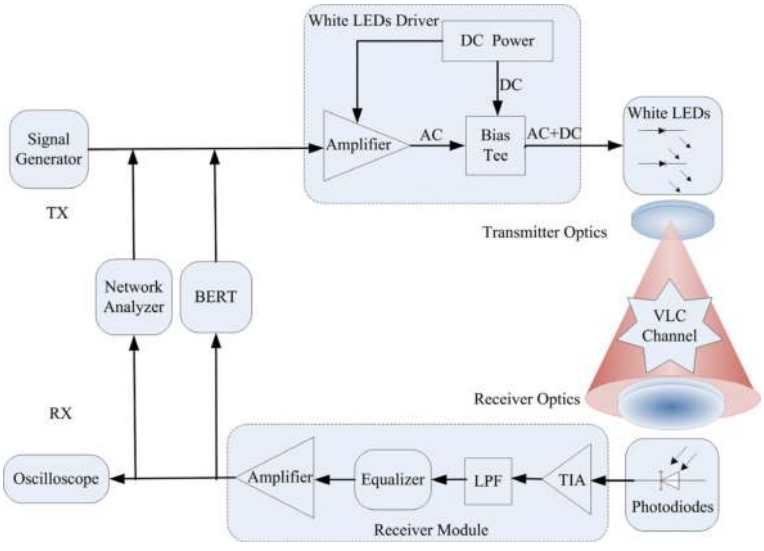

Figure 10. Experimental setup of visible light communication system using white LEDs.

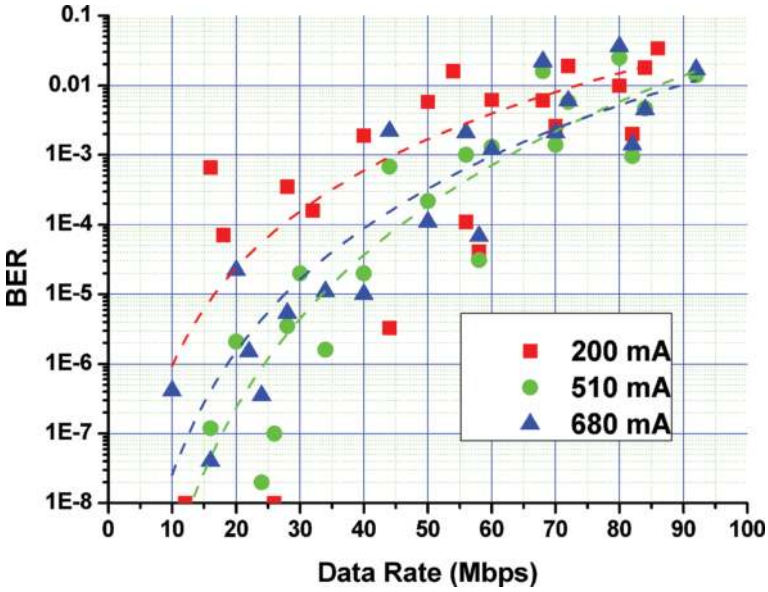

Figure 11. Relationship between VLC bit error rate and date rate for different LED DC-bias currents.

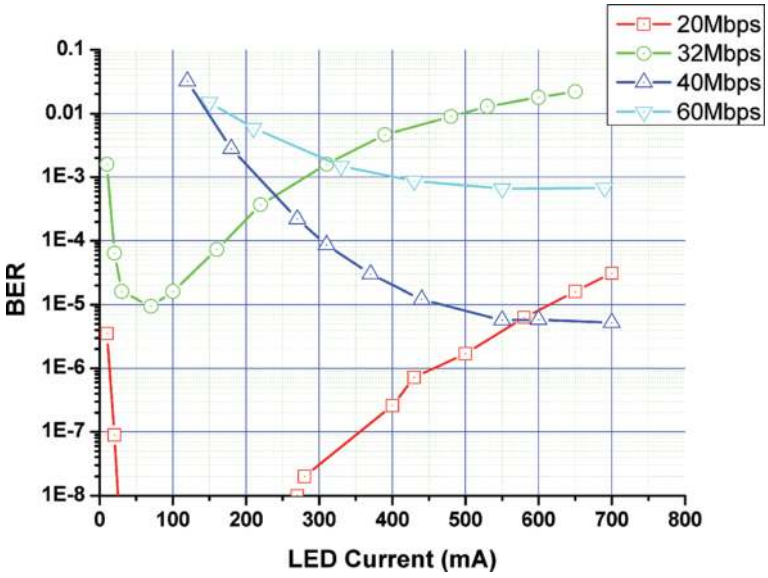

Figure 12. Relationship between VLC bit error rate and LED current for different date rate.

3. Real-time software-defined adaptive MIMO VLC system

3.1. System model of adaptive MIMO VLC

A MIMO visible light communication system consists of M transmitting antennas (LEDs) and N receiving antennas (photodetectors). The input data X are mapped by QAM and divided into M parallel symbol streams x_j ($j = 1,\ldots, M$) to independently modulate a light source. The transmitted signal after up-conversion takes the form [16]:

$$x(t) = I(t)\cos(2\pi f_c t) - Q(t)\sin(2\pi f_c t) \tag{7}$$

where f_c is the carrier frequency, $I(t)$ and $Q(t)$ are the modulating signals of in phase and quadrature components. The received signal is a linear combination of all x_j, and the MIMO channel model can be represented as [16]

$$\mathbf{y} = \mathbf{H}\mathbf{x} + \mathbf{n}, \tag{8}$$

where $\mathbf{n}$ is the sum of thermal noise and ambient shot light noise with zero mean and a variance σ^2, and the noise power spectral density is N_0. It is assumed that N_t data symbols x_1, x_2, …, x_{Nt} are chosen randomly, equally likely and independently to form an input data vector $\mathbf{x} = [x_1, x_2, \ldots, x_{N_t}]^T \in \mathbf{A}^M$ where $\mathbf{A}$ is a given modulation constellation. Each Tx transmits independent symbols of the same power: $<\mathbf{x}\mathbf{x}^*> = P_t/N_t.\mathbf{I}$, where P_t is the total Tx power, $\mathbf{I}$ is the identity matrix, <> and * denote the expectation and Hermitian conjugation, respectively. The received signal vector is denoted by $\mathbf{y} = [y_1, y_2, \ldots, y_{N_r}]^T$. Notation $\mathbf{H}$ denotes an $N_t \times N_r$ channel matrix, in which h_{nm} is the real nonnegative coefficient between the nth receiver and the mth transmitter.

Channel gain of an indoor VLC LOS link is determined by [28]

$$h_{nm} = \begin{cases} \dfrac{(k+1)A}{2\pi d_{nm}^2}\cos^k(\phi)\cos(\psi), & 0 \le \psi \le \Psi_{\frac{1}{2}} \\ 0, & \psi > \Psi_{\frac{1}{2}} \end{cases} \tag{9}$$

with ψ is the angle of incidence with respect to the nth receiver axis, and φ is the angle of emergence with respect to the mth transmitter axis. d_{nm} is the distance between mth transmitter and nth receiver. Ψ is the field-of-view (FOV) of the receiver, A is the detector area, and $k = -\ln 2/\ln(\cos(\varphi_{1/2}))$, in which $\varphi_{1/2}$ is the half power angle of the transmitter.

The MIMO system has first to estimate channel estimation coefficients between Tx and Rx, to de-multiplex signals and retrieve transmitted data. We periodically inserted training sequences of binary phase shift keying signals in front of the data streams to obtain the channel estimation matrix. Each row of the two-dimensional (2D) array contains two training sequences, one from each transmitter [16].

$$\mathbf{t} = \begin{pmatrix} ts_1 & 0 \\ 0 & ts_2 \end{pmatrix} \tag{10}$$

Thus, we can determine the four channel estimates by performing channel estimation on each training sequence in each row. An **H** matrix detailing channel estimation is logged on receiving all pilot signals $\mathbf{y_t}$.

$$\mathbf{H} = \frac{\mathbf{y_t}}{\mathbf{t}} = \begin{pmatrix} y_{11}/ts_1 & y_{12}/ts_2 \\ y_{21}/ts_1 & y_{22}/ts_2 \end{pmatrix} \tag{11}$$

Zero-forcing (ZF) is the simplest method to estimate the transmitted data, that invert **H** and multiply it with the received vector [29]: $\mathbf{W}^*\mathbf{y} = \mathbf{x}_{\text{est}} + \mathbf{n}$, where W is the beam former $\mathbf{H}^{-1}$. However, if **H** is rank deficient, matrix inversion cannot be performed. The noise vector **n** will lead to noise amplification for low values of **H**. Thus, the pseudo inverse of **H** can be used by [16]:

$$\mathbf{H}^{\dagger} = (\mathbf{H}^*\mathbf{H})^{-1}\mathbf{H}^*, \tag{12}$$

where **H*** is the conjugated transpose of **H**. Using the pseudo inverse zero-forcing, the demultiplexing and postequalization can be simultaneously realized for an estimate of **x**.

The adaptive MIMO is mainly based on the approximated expression for the average bit error rate (BER) of M-ary QAM symbols and channel capacity of the MIMO system. An approximate expression of average bit error probability of M-ary square QAM can be obtained by

$$P_b \cong \frac{2\left(\sqrt{M}-1\right)}{\sqrt{M}\log_2^M} erfc\left(\sqrt{\frac{3}{2(M-1)}\gamma}\right) \tag{13}$$

where γ is the received signal to noise ratio (SNR) per symbol, and $erfc(x)$ is the complementary error function. The analytical error-probability bound for an AWGN SISO channel with M-QAM modulation is given by [30]

$$P_b \le \frac{1}{5}\exp\left(-1.5\frac{\gamma}{M-1}\right) \tag{14}$$

Assuming that signals from individual LEDs are independently equipowered, and a channel matrix is perfectly known to the receiver [29], spectral efficiency of MIMO channels is obtained by

$$\begin{aligned} S &= \log_2\left[\det\left(\mathbf{I}_N + \frac{P_t}{N_t\sigma_0^2}\mathbf{H}\mathbf{H}^*\right)\right] \\ &= \sum_{i=1}^{N_m}\log_2\left(1+\frac{P_t}{N_t\sigma_0^2}\lambda_i^2\right) \\ &\le \log_2\left(1+\frac{P_t}{N_t\sigma_0^2}\|\mathbf{H}\|^2\right) \end{aligned} \tag{15}$$

where $N_m = \min(N_t, N_r)$, $\boldsymbol{\lambda} \triangleq \left[\lambda_1^2, \ldots, \lambda_{N_m}^2\right]^T$ is eigenvalue vector of $\mathbf{H}\mathbf{H}^*$, $\|\|$ denotes the Frobenius norm, $\|\mathbf{H}\|^2 = \sum_{i=1}^{N}\sum_{j=1}^{M}|h_{i,j}|^2$.

For a given BER_{tgt}, the maximum spectral efficiency can be obtained by

$$s = \log_2(1 + K\gamma) \tag{16}$$

where $K = \frac{-3}{2\ln(5BER_{tgt})}$.

The adaptive MIMO system can be defined by the constrained optimization problem.

$$\max_{\text{MIMO}, s_i, P_i} S = E_{\lambda}\left[\sum_{i=1}^{N_m} s_i(\boldsymbol{\lambda})\right] \tag{17}$$

subject to

$$E_{\lambda}\left[\sum_{i=1}^{N_m} P_i(\boldsymbol{\lambda})\right] \leq P_t \tag{18}$$

$$\text{BER}_i(\boldsymbol{\lambda}) \leq \text{BER}_{tgt} \tag{19}$$

$$M_i(\boldsymbol{\lambda}) \in \{M_0, M_1, \ldots, M_n\} \tag{20}$$

$$\text{MIMO}(\boldsymbol{\lambda}) \in \{SM, SD\} \tag{21}$$

$$P_i(\boldsymbol{\lambda}) \geq 0, s_i(\boldsymbol{\lambda}) \geq 0, i = 1, \ldots, N_m \tag{22}$$

Eq. (17) expresses the optimization strategy that maximizing the spectral efficiency by adapting the MIMO scheme, transmit rate s_i and power P_i in each subchannel. Eq. (18) shows that the average total transmit power cannot exceed P_t, and Eq. (19) requires that at any instant the BER in any subchannel must remain below a predetermined target level BER_{tgt}. We consider more practical discrete rate systems in Eq. (20), where we restrict the available constellation size M_i to a finite set of integers instead of any nonnegative real values. In particular, we use only square QAMs as the available component modulation schemes; i.e., $M_i = 4^i$, $i = 0, 1, \ldots, N$. Based on the conditions of MIMO channel estimations, we can adapt the MIMO schemes in Eq. (21) such as spatial multiplexing (SM) and spatial diversity (SD) to maximize the achievable spectral efficiency. Eq. (22) is the nonnegative constraint on power and rate.The expectation over $\boldsymbol{\lambda}$ in Eq. (17) implies that we assume the random process $\boldsymbol{\lambda}$ is ergodic. These enable the MIMO adaptation in the time domain and spatial domain.

3.2. Experimental setup of adaptive MIMO VLC system

Figure 13 presents a block diagram and experimental setup of this 2 × 2 M-QAM adaptive MIMO VLC system. The random binary data is generated in Labview and would be first split into two parallel streams, one for each transmitter (TX) channel. We develop adaptive MIMO modes control modules, which can adjust the optimal modulation formats and MIMO schemes to maximize the spectral efficiency and error performance according to the real-time MIMO channel conditions. We adaptively choose one of MIMO technologies: spatial diversity (SD) and spatial multiplexing (SM). SD MIMO transmits the same data stream in each Tx to

improve antenna array gain, while SM MIMO sends different parallel streams over each LED to enhance spectral efficiency gain. Bit stream is mapped into *M*-ary QAM in each channel, and four types of modulation formats are provided: 4-QAM, 16-QAM, 64-QAM, and 256-QAM. Thus, there are eight adaptive MIMO modes available for link adaptation (SM-4, SM-16, SM-64, SM-256, SD-4, SD-16, SD-64, and SD-256). Initially, we choose the default mode of SM-64 (spatial multiplexing 64-QAM). Then channel-training sequences are inserted into the symbol streams. After adding cyclic prefix (CP) and upsampling, pulse shaping by a raised-cosine filter is employed.

Data streams are transmitted from the host computer to USRP X310 using 10G SFP+ Ethernet interfaces. The complex QAM streams are upconverted after digital to analog conversion (DAC), and generate the real analogue RF signals. The analogue transmitter front end superimposed the amplified output signal onto LED bias current using a bias tee. The phosphorescent white LED (Osram OSTAR) with four chips provided 520-lm luminous flux with a 120° opening angle at 700 mA current. An aspheric lens collimated LED light propagation along line-of-sight direction. A high-speed PIN photodetector captured LED light by an aspheric convex lens. A low noise transimpedance amplifier (TIA) amplified the photocurrent signal, which bandwidth was extended by a first-order analogue postequalizer.

Subsequently, we routed the received signals from each receiver to an RX channel of USRP X310. USRP X310 is a scalable software-defined radio (SDR) platform for designing and deploying the next generation wireless communication system. The hardware architecture integrates two daughterboard slots covering DC-6 GHz with up to 120 MS/s of baseband bandwidth, 200 MS/s ADC, and 800 MS/s DAC, and dual high-speed SFP(+) interface ports for 1/10 Gigabit Ethernet. We set 10 MHz baseband bandwidth due to the limited sampling

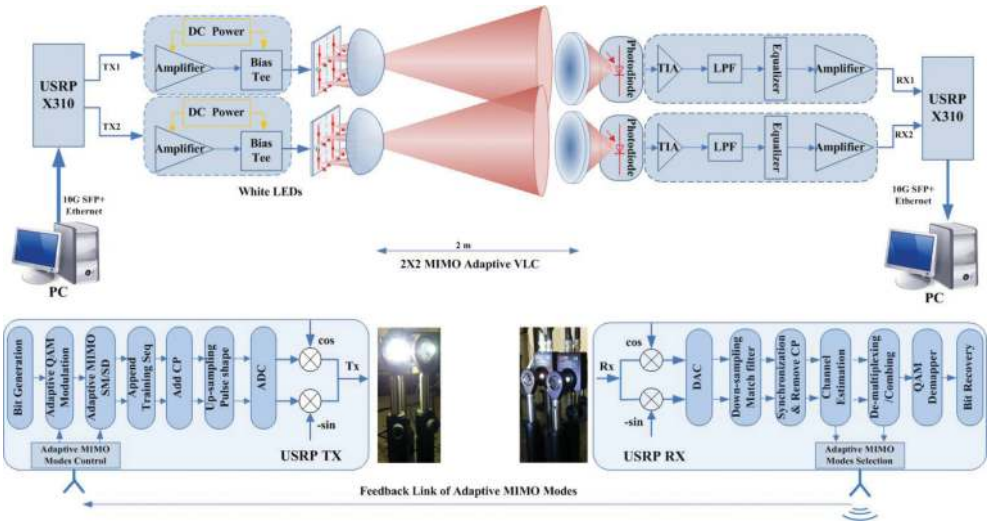

Figure 13. Experiment setup for adaptive MIMO VLC.

rate of daughterboard and analog to digital conversion (ADC). A large user-programmable Kintex-7 FPGA in a convenient desktop provides best-in-class real-time hardware performance [16].

Training sequences are acquired for synchronization and channel estimation, after downconverting to baseband and down sampling by a matched filter. With removing CP, the received data streams are processed in an MIMO de-multiplexer. The final streams are then passed through a QAM demodulator to recover original binary streams. Based on the channel estimation conditions, the adaptive MIMO mode selection module will calculate and select the corresponding optimum modes including modulation formats and MIMO schemes. We then update the three-bit binary code for adaptive MIMO modes and feedback the adaptive mode code to the transmitter by using RF uplink. In Labview, we measured and analyzed the constellation diagram, EVM, BER, and spectral efficiency performance for adaptive *M*-QAM MIMO VLC system.

4. Results and discussion

In order to achieve adaptive MIMO visible light communication for indoor lighting environment, we first evaluate efficient estimation approaches to acquire the real-time channel conditions. Then we measured and compared the error performance and spectral efficiency of M-QAM MIMO VLC systems using spatial diversity and spatial multiplexing, respectively. Based on the adaptive MIMO mode selection criteria in terms of channel estimation, we demonstrated the adaptive real-time software-defined MIMO VLC along with different distance.

4.1. Real-time single-carrier QAM MIMO visible light communication

Figure 14(a) shows the captured waveforms and resulting IQ symbols of RX1 and RX2 for 64-QAM spatial diversity MIMO VLC. From this figure, we can find the crosstalk and phase offset between these two RXs, which require MIMO processing in the DSP. The constellation plots show the signals received by the two Rx NI USRP transceivers.

We recover 2D array of symbols by postequalization with channel estimations and convert them into the proper 1D array of symbols by performing max ratio combining (MRC) as shown in **Figure 6(b)**.

Figure 14(c) and **(d)** shows the recovered signal constellation diagram after channel equalization. **Figure 14(e)** shows the final MIMO combined signal constellation plot after performing max ratio combing (MRC). The measured root mean square (RMS) EVM and BER are 1.73% and zero, respectively. This reconstructed constellation shows that MIMO system works properly.

We then demonstrate spatial multiplexing MIMO VLC by transmitting different data streams. **Figure 15(a)** shows four received I and Q waveforms from each of the two Rx antennas after downsampling and postequalization, which are combined together by MIMO de-multiplexing to recover the MIMO RX symbols IQ graph in **Figure 15(b)**. From **Figure 14(c)–(e)**, we can find

that all the 64-QAM IQ symbol waveforms have been successfully reconstructed in the spatial multiplexing MIMO VLC system. Furthermore, we measured high-order modulation performance for 256-QAM spatial multiplexing MIMO VLC, which constellation diagrams are depicted in **Figure 16**. The results show clear constellations and error free transmission in 256-QAM spatial multiplex 2 × 2 MIMO VLC with EVM 1.81%, BER 2 × 10^{-5} and data rate 160 Mbps along 2 m.

Figure 17 shows comparison of BER versus signal power of a 64-QAM 2 × 2 MIMO VLC transmission. Compared with spatial multiplexing, the spatial diversity MIMO VLC system can enhance about 3-dB array gain in BER performance, as the array gain in spatial diversity MIMO VLC improves the received signal strength.

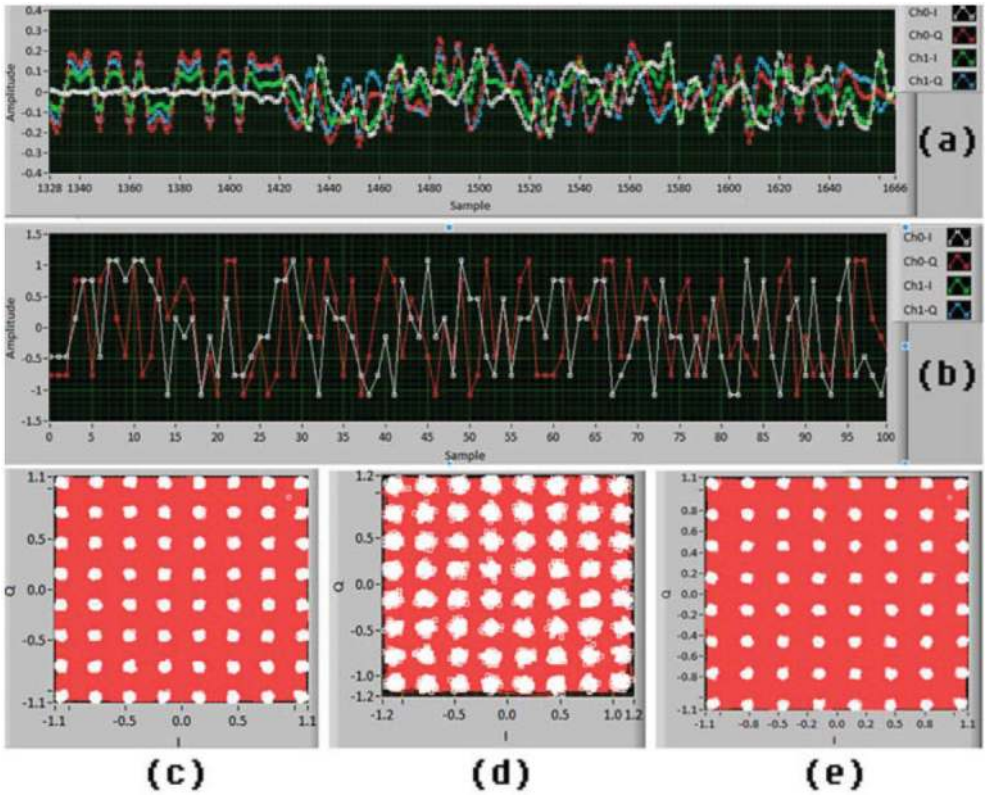

Figure 14. Spatial diversity 64-QAM 2 × 2 MIMO VLC. (a) Rx waveform IQ graph, (b) RX MIMO MRC combined symbol IQ graph, (c) RX CH0 constellation diagram, (d) RX CH1 constellation diagram, and (e) MIMO combined signal after max ratio combing diagram.

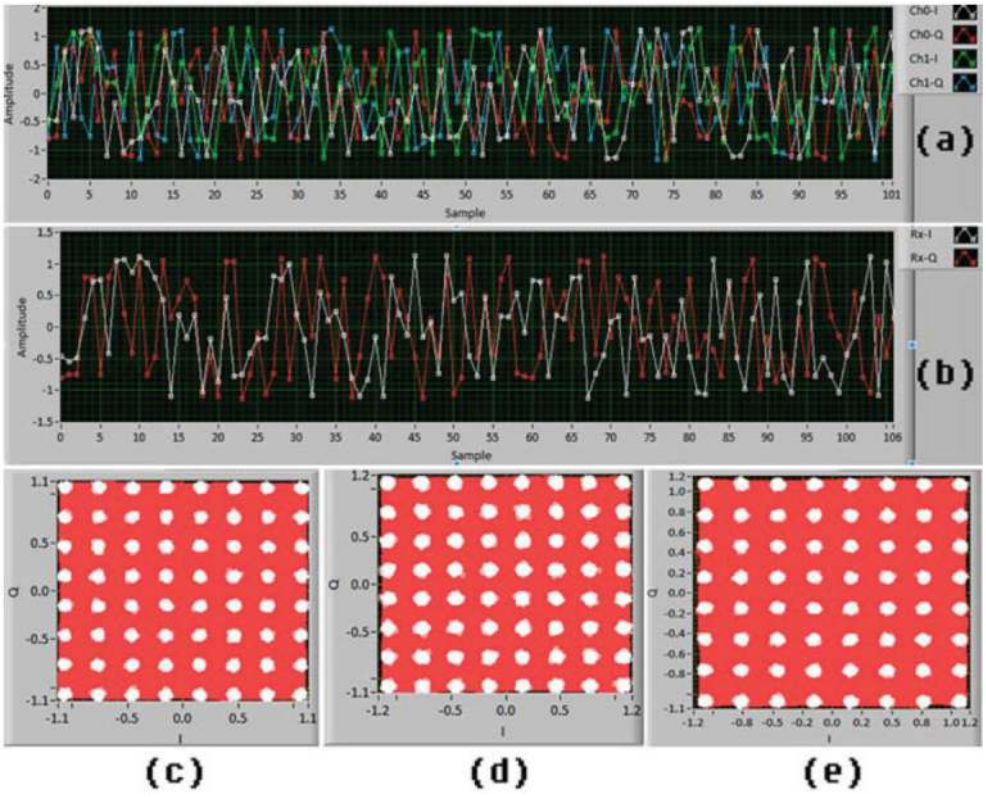

Figure 15. Spatial multiplexing 64-QAM 2 × 2 MIMO VLC. (a) Rx waveform IQ graph, (b) RX MIMO IQ graph, (c) RX CH0 constellation diagram, (d) RX CH1 constellation diagram, and (e) Rx MIMO spatial multiplexing diagram, EVM = 1.89%, BER = 0.

4.2. Software-defined MIMO VLC using link adaptation of spatial diversity and spatial multiplexing

Figure 18 shows the measured EVM and channel response estimation against signal power for 2 × 2 MIMO 4-QAM VLC using spatial multiplexing and spatial diversity. For large symbol streams T, such that $T \gg N$, where N is the number of unique modulation symbols, channel SNR can be obtained from EVM as $\text{SNR} \approx 1/\text{EVM}^2$. As shown in **Figure 10**, EVM of SM and SD MIMO VLC decreases correspondingly with an increase of signal power. As EVM approaches to small value of 2%, both EVMs become saturated due to the limited symbols streams. It is clear that EVM of spatial diversity system has a power gain of about 3 dB compared to the spatial multiplexing due to the antenna array gain. Channel SNR estimation from the measured EVM is dependent on the symbol number, constellation size, and MIMO processing. On the other hand, we obtain channel SNR directly from a channel response estimation matrix,

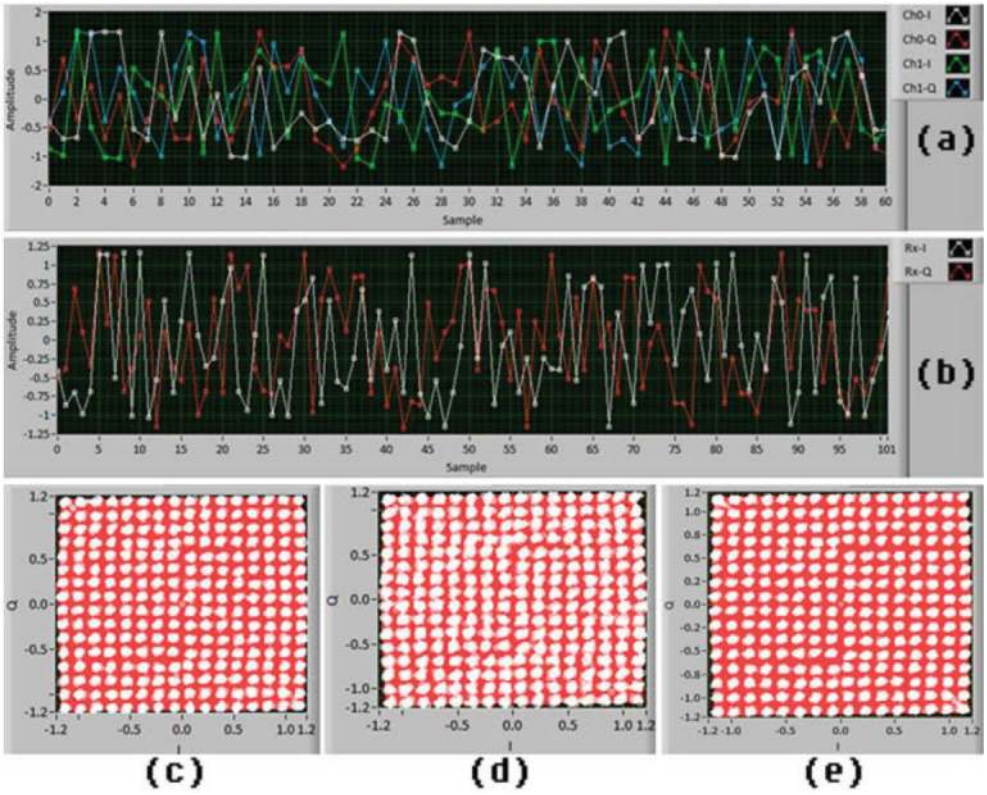

Figure 16. Spatial multiplexing 256-QAM 2 × 2 MIMO VLC. (a) Rx waveform IQ graph, (b) RX MIMO IQ graph, (c) RX CH0 constellation diagram, (d) RX CH1 constellation diagram, and (e) Rx MIMO spatial multiplexing diagram, EVM = 1.81%, BER = 2E-5.

where λ_i is eigenvalue of channel estimation matrix H. As **Figure 10** shows, each subchannel eigenvalue of channel estimation has a linear relationship with signal power. Furthermore, original channel estimation matrix is similar for both spatial diversity and spatial multiplexing MIMO. Thus, we can acquire real-time subchannel SNRs from eigenvalues of channel estimation matrix regardless of MIMO schemes and modulation formats.

BER performance of 4-16-64-256 QAM 2 × 2 MIMO VLC using spatial multiplexing and spatial diversity is shown in **Figure 19**, where dots are experimental measurements and lines are theoretical results. The results show that BER decreases significantly to 10^{-7} as SNR grows with a linear dynamic range. Moreover, no nonlinear distortion occurs at high signal power by using single-carrier M-QAM modulation for the 2 × 2 MIMO VLC system. We can see that BER of spatial diversity system has about 3-dB SNR gain compared to the spatial multiplexing, as the array gain in spatial diversity MIMO VLC improves the received signal strength. It is clear that the experimental measurements well match the theoretical results, which verify

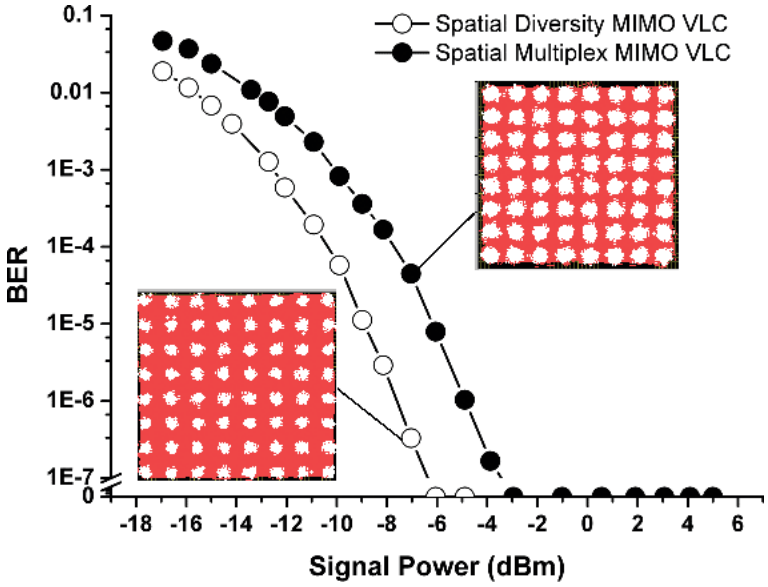

Figure 17. BER performance comparison for spatial diversity and spatial multiplex 64-QAM 2 × 2 MIMO VLC.

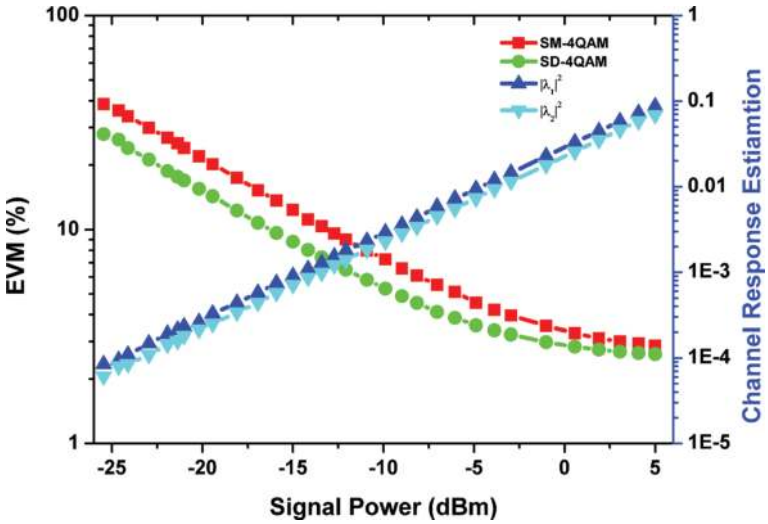

Figure 18. EVM and channel estimation against signal power for 2 × 2 MIMO VLC using spatial multiplexing (SM) and spatial diversity (SD).

accurate channel SNR estimation from the channel matrix in M-QAM MIMO VLC. Given the target BER threshold $BER_{tgt} = 10^{-3}$, we can establish adaptive MIMO mode criteria in terms of channel SNR and singular value of channel matrix.

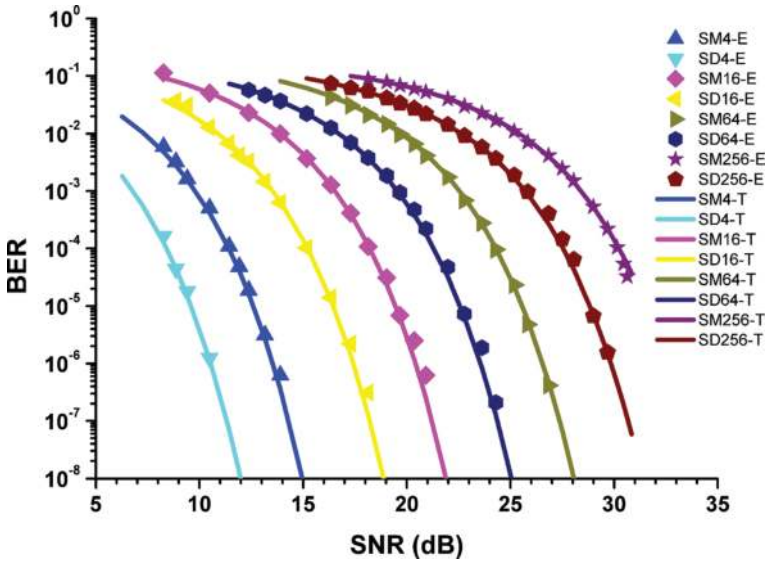

Figure 19. BER performance of M-QAM 2 × 2 MIMO VLC using spatial multiplexing and spatial diversity. Dots are experimental results and lines are theoretical results.

Figure 20 shows spectral efficiency performance of 4-16-64-256 QAM 2 × 2 MIMO VLC using spatial multiplexing and spatial diversity, where dots are experimental results and lines are theoretical results. Insets show the corresponding constellation diagrams. The results show spectral efficiencies of M-QAM MIMO VLC form step like shapes due to the rate discretization and BER integration. We can see that the spatial multiplexing system has about 3 dB gain in spectral efficiency compared with spatial diversity due to multiplexing gain of SM. These bandwidth efficiency enhancements are at the scarification of the degraded error performance. The experimental measurements well match the theoretical results, which verify channel SNR estimation and of spectral efficiency of M-QAM MIMO VLC. Thus, we can establish the adaptive MIMO mode criteria in terms of singular value of channel matrix to maximize the spectral efficiency.

Based on the established adaptive MIMO mode criteria in terms of channel estimation as shown in **Figure 21**, we demonstrate the real-time adaptive MIMO VLC system to maximize spectral efficiency under target BER threshold. BER performance and spectral efficiency against link distance for adaptive M-QAM MIMO VLC are depicted in **Figures 22** and **23**, respectively. The fixed 64-QAM MIMO VLC using spatial diversity and spatial multiplexing are introduced for comparison. Insets show the corresponding constellations of adaptive MIMO modes.

The initial mode is SM-64 (spatial multiplex 64-QAM). As we can see in the figures, as link distance increases from 0.6 to 1.4 m and 1.9 m, the adaptive modes change to SM-256, SM-64 and SM-16, receptively. Adaptive MIMO VLC increases the error free transmission distance to 2.2 m compared with 1.7 m for SM-64 and 1.9 m for SD-64. Furthermore, adaptive MIMO

http://dx.doi.org/10.5772/intechopen.68919

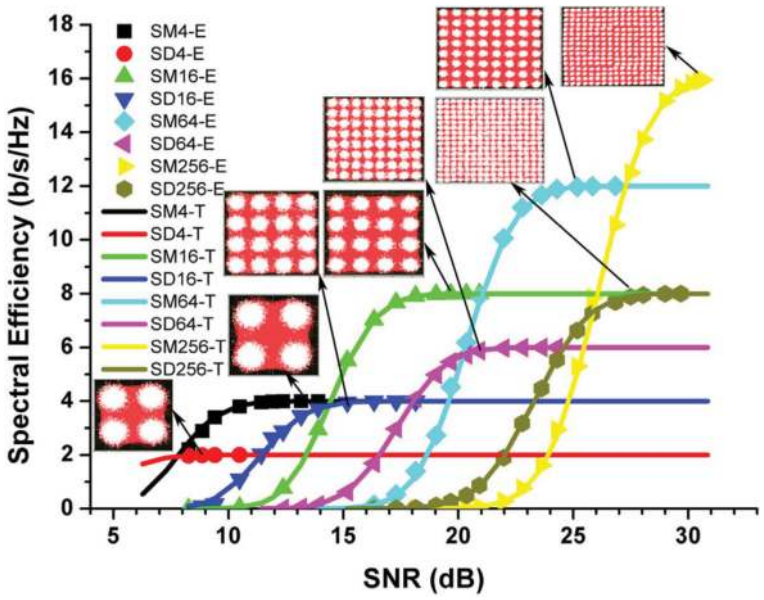

Figure 20. Spectral efficiency performance of M-QAM 2 × 2 MIMO VLC using spatial multiplexing and spatial diversity. Dots are experimental results and lines are theoretical results. Insets are the corresponding constellation diagrams.

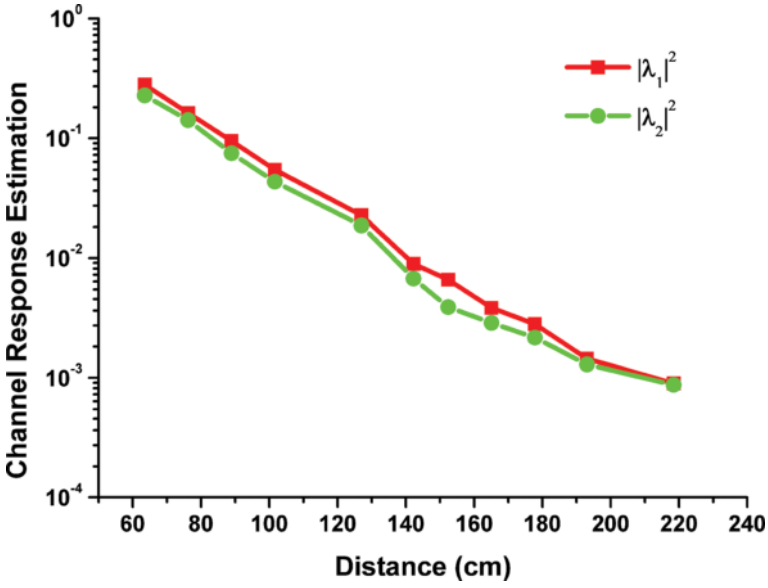

Figure 21. Channel estimation against link distance for 2 × 2 M-QAM MIMO VLC.

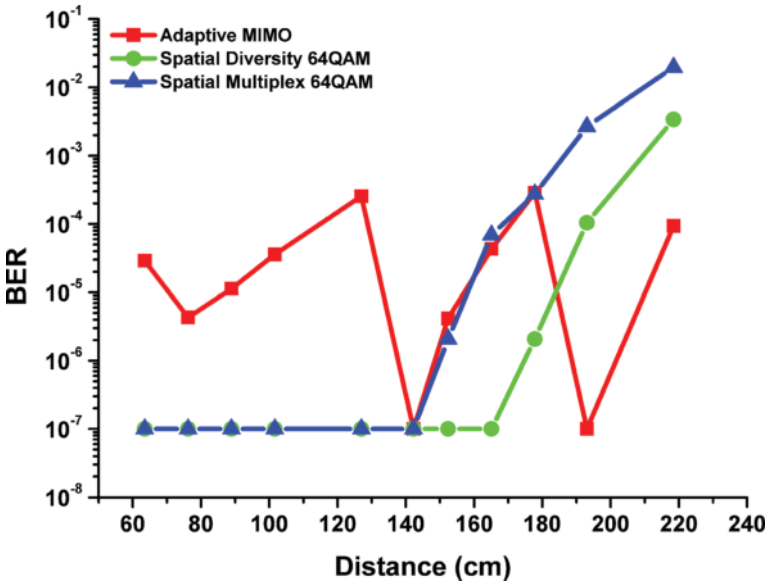

Figure 22. BER against link distance for adaptive M-QAM MIMO, spatial multiplexing 64-QAM, and spatial diversity 64-QAM VLC.

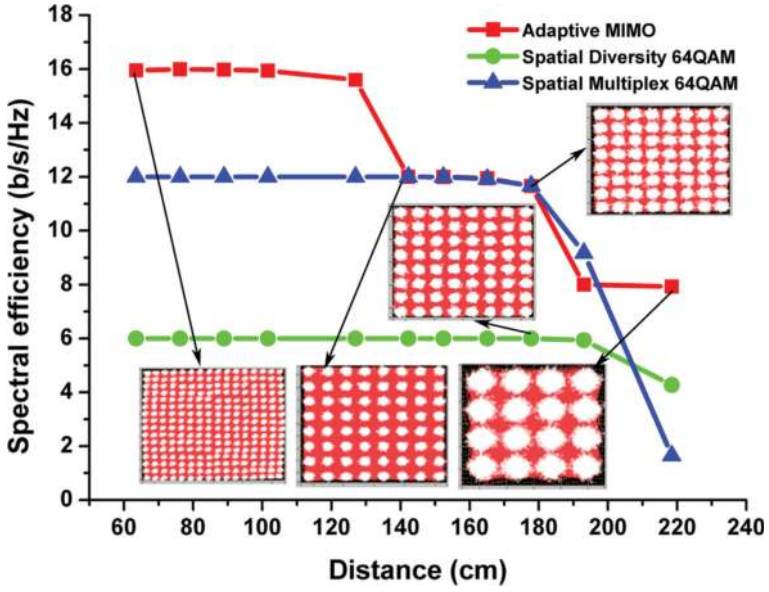

Figure 23. Spectral efficiency against link distance for adaptive M-QAM MIMO, spatial multiplexing 64-QAM, and spatial diversity 64-QAM VLC.

VLC enhances the average spectral efficiency to 12 b/s/Hz over 2.2 m distance. Thus, it is necessary to explore the optimal combination of spatial multiplexing and spatial diversity for adaptive MIMO VLC to improve spectral efficiency and BER performance for indoor lighting environment.

4.3. Adaptive software-defined MIMO VLC after a mobile obstruction

Based on the established adaptive MIMO mode criteria in terms of channel estimation matrix, we demonstrate the real-time adaptive MIMO VLC system to maximize spectral efficiency under target BER threshold, after propagation beyond an obstruction. An obstacle with a diameter of 4.5 cm placed in the middle of transmission distance of 218 cm obstructs the line-of-sight light waves from two LEDs separated by 5 cm. We marked the central line between the two LEDs as a reference position at 0 cm. The obstacle was translated across the line-of-sight transmission direction from −65 to 65 cm, with dynamical obstruction range of 135 cm.

With the obstacle moving across LOS links, we measured the channel response of subchannels in **Figure 24**, and compared the error performance and spectral efficiency of adaptive M-QAM MIMO VLC with traditional MIMO VLC as shown in **Figures 25** and **26**. The fixed 64-QAM MIMO VLC using spatial diversity and spatial multiplexing are introduced for comparison. Insets show the corresponding constellations of adaptive MIMO modes. The initial mode is SM-64 (spatial multiplex 64-QAM). As we can see in the figures, as the obstacle moved across LOS from −65 to 65 cm, the adaptive MIMO modes change to SM-256, SM-64 and SD-256 adaptively with BER less than 10^{-3}. Results show that adaptive MIMO VLC can overcome these losses by the blockage, thus recover the clear constellation diagrams after propagation

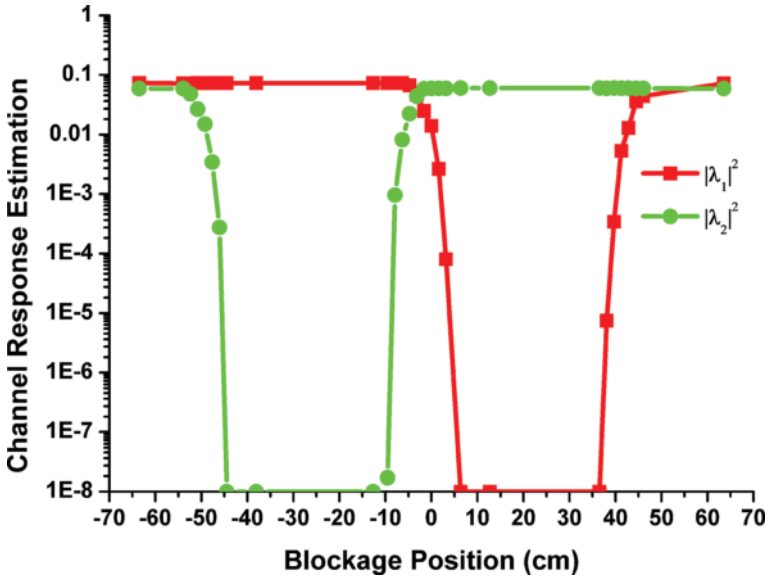

Figure 24. Channel estimation against blockage position for 2 × 2 M-QAM MIMO VLC.

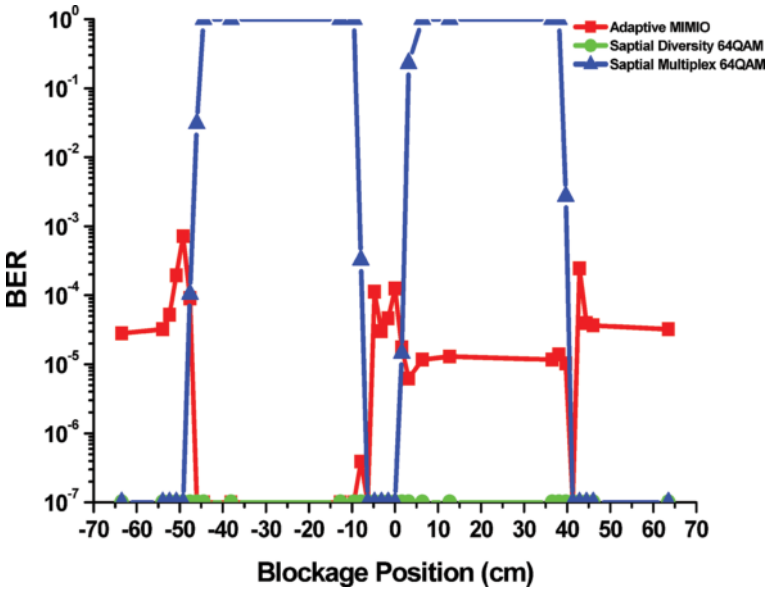

Figure 25. BER against blockage position for adaptive M-QAM MIMO VLC, spatial multiplexing 64-QAM, and spatial diversity 64-QAM VLC.

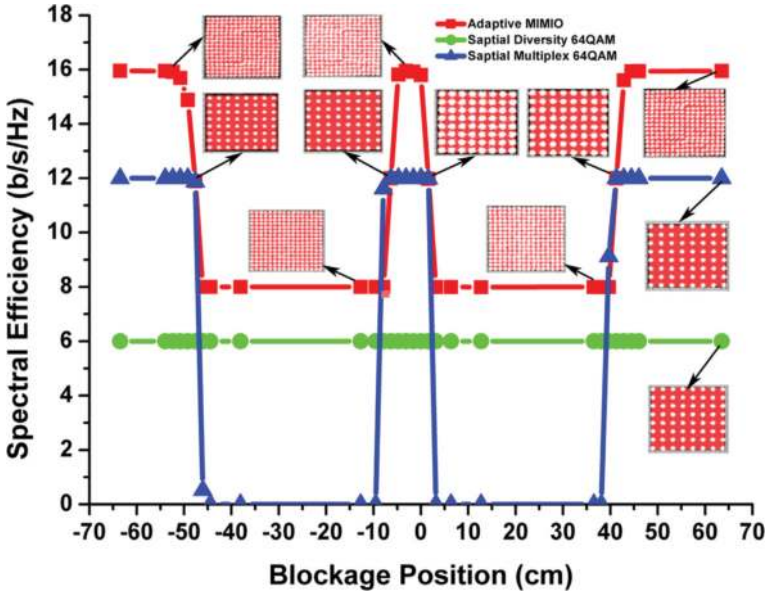

Figure 26. Spectral efficiency against blockage position for adaptive M-QAM MIMO VLC, spatial multiplexing 64-QAM, and spatial diversity 64-QAM VLC.

beyond the obstruction. Adaptive MIMO VLC enhanced the average error-free spectral efficiency to 12 b/s/Hz over 2-m indoor transmission with an obstruction, compared with 7.7 b/s/Hz for SM-64 and 6 b/s/Hz for SD-64. The adaptive MIMO VLC will enhance spectral efficiency and error performance in a real-time combined lighting and communication environment such as transmission power distribution, environmental blockage, and shadowing.

5. Conclusion

In this chapter, we experimentally demonstrate real-time software-defined multiple-input multiple-output (MIMO) visible light communication (VLC) system employing link adaptation of spatial multiplexing and spatial diversity. Real-time MIMO signal processing is implemented by using the field programmable gate array (FPGA)-based universal software radio peripheral (USRP) devices. Software-defined implantation of MIMO VLC can assist in enabling an adaptive and reconfigurable communication system without hardware changes. We propose the adaptive MIMO solution that both modulation schemas and MIMO schemas are dynamically adapted to the changing channel conditions for enhancing the error performance and spectral efficiency. The average error-free spectral efficiency of adaptive 2×2 MIMO VLC achieved 12 b/s/Hz over 2 m indoor dynamic transmission. The adaptive MIMO VLC will enhance performance in a real-time combined lighting and communication environment such as transmission power distribution, beam forming, communication range, environmental blockage, and shadowing.

Acknowledgements

This work has been funded by the National Science Foundation (NSF) ECCS directorate under projects Award #1201636 and Award #1160924.

Author details

Peng Deng

Address all correspondence to: dptyleo@gmail.com

Department of Electrical Engineering, The Pennsylvania State University, University Park, USA

References

[1] Kavehrad M. Sustainable energy-efficient wireless applications using light. IEEE Communications Magazine. 2010;**48**(12):66–73. DOI: 10.1109/Mcom.2010.5673074

[2] O'Brien D, Parry G, Stavrinou P. Optical hotspots speed up wireless communication. Nature Photonics. 2007;**1**(5):245–247. DOI: 10.1038/nphoton.2007.52

[3] Honglei L, Xiongbin C, Beiju H, Danying T, Hongda C. High bandwidth visible light communications based on a post-equalization circuit. Photonics Technology Letters, IEEE. 2014;**26**(2):119–122. DOI: 10.1109/LPT.2013.2290026

[4] Tsonev D, Chun H, Rajbhandari S, McKendry JJD, Videv S, Gu E, et al. A 3-Gb/s single-LED OFDM-based wireless VLC link using a gallium nitride μLED. Photonics Technology Letters, IEEE. 2014;**26**(7). DOI: 637–40. 10.1109/LPT.2013.2297621

[5] Wang Y, Tao L, Huang X, Shi J, Chi N. 8-Gb/s RGBY LED-Based WDM VLC System Employing High-Order CAP Modulation and Hybrid Post Equalizer. Ieee Photonics J. 2015;**7**(6):1–8. 10.1109/jphot.2015.2489927

[6] Neokosmidis I, Kamalakis T, Walewski JW, Inan B, Sphicopoulos T. Impact of Nonlinear LED Transfer Function on Discrete Multitone Modulation: Analytical Approach. Journal of Lightwave Technology. 2009;**27**(22):4970–78. DOI 10.1109/Jlt.2009.2028903

[7] Deng P, Kavehrad M, Kashani MA. Nonlinear modulation characteristics of white LEDs in visible light communications. In: Optical Fiber Communication Conference; 22–26 March 2015; Los Angeles, CA. 2015. p. W2A.64. DOI: 10.1364/OFC.2015.W2A.64

[8] Deng P, Kavehrad M, Liu Z, Zhou Z, Yuan X. Capacity of MIMO free space optical communications using multiple partially coherent beams propagation through non-Kolmogorov strong turbulence. Optics Express. 2013;**21**(13):15213–29.

[9] Azhar AH, Tran T, O'Brien D. A gigabit/s indoor wireless transmission using MIMO-OFDM visible-light communications. Photonics Technology Letters, IEEE. 2013;**25**(2):171–174. DOI: 10.1109/LPT.2012.2231857

[10] Burton A, Minh HL, Ghassemlooy Z, Bentley E, Botella C. Experimental Demonstration of 50 Mb/s Visible Light Communications using 4×4 MIMO. IEEE Photonic Tech L. 2014;**20**(9):945–8. DOI: 10.1109/LPT.2014.2310638

[11] Wang YQ, Chi N. Demonstration of high-speed 2 x 2 non-imaging MIMO Nyquist single carrier visible light communication with frequency domain equalization. Journal of Lightwave Technology. 2014;**32**(11):2087–2093. DOI: 10.1109/Jlt.2014.2320306

[12] Deng P, Yuan X, Kavehrad M, Zhao M, Zeng Y. Off-axis catadioptric fisheye wide field-of-view optical receiver for free space optical communications. Optical Engineering. 2012;**51**(6):063002.

[13] Te C, Lu L, Bo T, Zhong Z, Weiwei H. High-spatial-diversity imaging receiver using fisheye lens for indoor MIMO VLCs. Photonics Technology Letters, IEEE. 2014;**26**(22):2260–2263. DOI: 10.1109/LPT.2014.2354458

[14] Cui K, Chen G, Xu Z, Roberts RD. Line-of-sight visible light communication system design and demonstration. Communication Systems Networks and Digital Signal Processing

(CSNDSP), 2010 7th International Symposium on; July 21–23, 2010; Newcastle upon Tyne, UK. p. 621–5.

[15] Gu WJ, Aminikashani M, Deng P, Kavehrad M. Impact of multipath reflections on the performance of indoor visible light positioning systems. Journal of Lightwave Technology. 2016;**34**(10):2578–25787. DOI: 10.1109/Jlt.2016.2541659

[16] Deng P, Kavehrad M. Real-time software-defined single-carrier QAM mimo visible light communication system. 2016 Integrated Communications Navigation and Surveillance (ICNS); 19–21 April 2016; Herndon, VA. IEEE;2016. p. 5A3–5. DOI: 10.1109/ICNSURV.2016.7486354

[17] Deng P, Kavehrad M. Software Defined Adaptive MIMO Visible Light Communications after an Obstruction. Optical Fiber Communication Conference; 19-23 March 2017; Los Angeles, CA. OSA;2017. p. Th1E.5. DOI: 10.1364/OFC.2017.Th1E.5

[18] Rahaim M, Miravakili A, Ray S, Koomson V, Hella M, Little T. Software defined visible light communication. Wireless Innovation Forum Conference on Communications Technologies and Software Defined Radio (WInnComm SDR); 11-13 March, 2014. Schaumburg, Illinois.

[19] Deng P, Kavehrad M, Lou Y. MEMS-based beam-steerable free-space optical communication link for reconfigurable wireless data center. SPIE OPTO; January 28, 2017; San Francisco, CA; 2017. pp. 1012805–9.

[20] Deng P, Kavehrad M. Adaptive Real-Time Software Defined MIMO Visible Light Communications using Spatial Multiplexing and Spatial Diversity. Wireless for Space and Extreme Environments (WiSEE), 2016 IEEE International Conference on; 26–29 September 2016; Aachen, Germany. IEEE; 2016. p. 111–116. DOI: 10.1109/WiSEE.2016.7877314

[21] Zhang R, Wang J, Wang Z, Xu Z, Zhao C, Hanzo L. Visible light communications in heterogeneous networks: Paving the way for user-centric design. IEEE Wireless Communications. 2015;**22**(2):8–16. DOI: 10.1109/MWC.2015.7096279

[22] Elgala H, Mesleh R, Haas H. An LED model for intensity-modulated optical communication systems. IEEE Photonic Technology Letters. 2010;**22**(11):835–7. DOI: 10.1109/Lpt.2010.2046157

[23] Deng P, Kavehrad M. Effect of white LED DC-bias on modulation speed for visible light communications. arXiv preprint arXiv:161208477. 2016.

[24] Schubert EF, Gessmann T, Kim JK. Light emitting diode. 2nd ed. New York: Cambridge University Press; 2006. 422 p. DOI: 10.1017/CBO9780511790546

[25] Green RP, McKendry JJD, Massoubre D, Gu ED, Dawson MD, Kelly AE. Modulation bandwidth studies of recombination processes in blue and green InGaN quantum well micro-light-emitting diodes. Applied Physics Letters. 2013;**102**(9):1–4. Doi 10.1063/1.4794078

[26] Galler B, Drechsel P, Monnard R, Rode P, Stauss P, et al. Influence of indium content and temperature on Auger-like recombination in InGaN quantum wells grown on (111) silicon substrates. Applied Physics Letters. 2012;**101**(13):1–4. DOI: 10.1063/1.4754688

[27] Schubert EF, Hunt NEJ, Malik RJ, Micovic M, Miller DL. Temperature and modulation characteristics of resonant-cavity light-emitting diodes. Journal of Lightwave Technology. 1996;**14**(7):1721–1729. DOI: 10.1109/50.507950

[28] Komine T, Nakagawa M. Fundamental analysis for visible-light communication system using LED lights. IEEE Trans/actions on Consumer Electronics. 2004;**50**(1):100–107.

[29] Oestges C, Clerckx B. MIMO wireless communications: From real-world propagation to space-time code desig. Orlando: Academic Press; 2010. 480 p.

[30] Zhou ZD, Vucetic B, Dohler M, Li YH. MIMO systems with adaptive modulation. IEEE on Transactions on Vehicular Technology. 2005;**54**(5):1828–1842. DOI: 10.1109/tvt.2005.853886